

Multimodal Densenet

Faisal Mahmood¹, Ziyun Yang^{1,2}, Thomas Ashley¹ and Nicholas J. Durr¹

¹Department of Biomedical Engineering, Johns Hopkins University, Baltimore, MD

²Beijing Institute of Technology, Beijing, China

{faisalm,ndurr}@jhu.edu

Abstract

Humans make accurate decisions by interpreting complex data from multiple sources. Medical diagnostics, in particular, often hinge on human interpretation of multimodal information. In order for artificial intelligence to make progress in automated, objective, and accurate diagnosis and prognosis, methods to fuse information from multiple medical imaging modalities are required. However, combining information from multiple data sources has several challenges, as current deep learning architectures lack the ability to extract useful representations from multimodal information, and often simple concatenation is used to fuse such information. In this work, we propose Multimodal DenseNet, a novel architecture for fusing multimodal data. Instead of focusing on concatenation or early and late fusion, our proposed architectures fuses information over several layers and gives the model flexibility in how it combines information from multiple sources. We apply this architecture to the challenge of polyp characterization and landmark identification in endoscopy. Features from white light images are fused with features from narrow band imaging or depth maps. This study demonstrates that Multimodal DenseNet outperforms monomodal classification as well as other multimodal fusion techniques by a significant margin on two different datasets.

1. Introduction

Humans have evolved complex neurological machinery to make adept decisions based on information from many diverse sources of data. This process is critical for characterizing many medical conditions, where a diagnostic work-up may depend on information from patient history, physical examination, organ-level medical imaging, histological analysis, and laboratory studies. Even in a single medical imaging study, physicians commonly rely on multimodal contrast to determine an optimal diagnosis, for instance, considering both T1- and T2-weighted MRI images

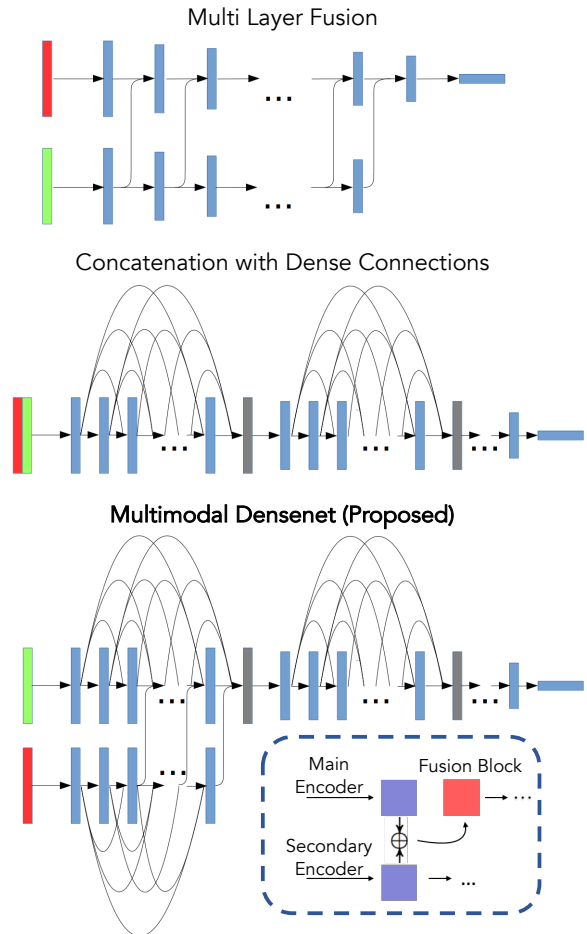


Figure 1. A comparison of commonly used multimodal deep learning architectures with the proposed architecture. The state-of-the-art methods involve multi-layer fusion [9, 13] or concatenation [29, 33]. We propose using a densenet style architecture and fusing the multimodal information in the last eight layers of the first dense block, hence harnessing the benefits of both multi-layer fusion and densely connected networks.

for identifying brain abnormalities. In screening for neoplasia in Barretts esophagus, a gastroenterologist can improve detection rates and decrease false positive findings by se-

quentially imaging the same tissue with high-resolution endoscopy, autofluorescence imaging, and narrow-band imaging [4]. Though the scenarios in which multimodal imaging are currently required and may stand the most to benefit from computer aided decision support, machine learning tools that effectively combine information from disparate sources remain immature and strategies for the optimal fusion of features from multimodal images is an active area of research.

Contributions.

- **DenseNet-based Multimodal Fusion:** We investigate a solution to fuse information from multiple modalities for more accurate scene classification in medical imaging applications. For this sake we propose a new architecture called Multimodal Densenet which is capable of fusing information from multiple modalities in a manner that fully harnesses dependencies between modalities and avoids common problems with vanishing gradients in multimodal networks. Our proposed architecture utilizes the strength of Densenet to tackle the vanishing gradients problem and the first block of dense layers fuses the two sources of data (Fig. 1).
- **Unpaired Multimodal Data:** We further demonstrate that unpaired multimodal information from the same scene or organ can be aligned using adversarial training via a dual-GAN framework with cycle-consistency loss.
- **Quantitative Study:** We comparatively analyze and quantitatively benchmark our proposed architecture with existing multimodal fusion architectures for scene classification such as modified version of FuseNet [9] and RedNet [13] and demonstrate that our proposed architecture outperforms these methods for two different datasets. We present state-of-the-art results for lesion classification and anatomical landmark identification in colonoscopy, with data sources of white light endoscopy, narrow-band imaging, and depth.

2. Related Work

Multimodal Deep Learning.

Multimodal machine learning continues to be an active research field with a variety of applications [2]. A major focus in early multimodal machine learning was on machine translation between visual data (e.g. images or video) and lingual data (e.g. audio or text) [26, 39]. Later, Socher *et. al.* demonstrated that multimodal feature modeling could be used to identify objects that a model had never seen before [37]. As convolutional neural networks (CNNs) became popular for image classification [16], they also started being used in multimodal tasks such as image captioning and text based image retrieval [15].

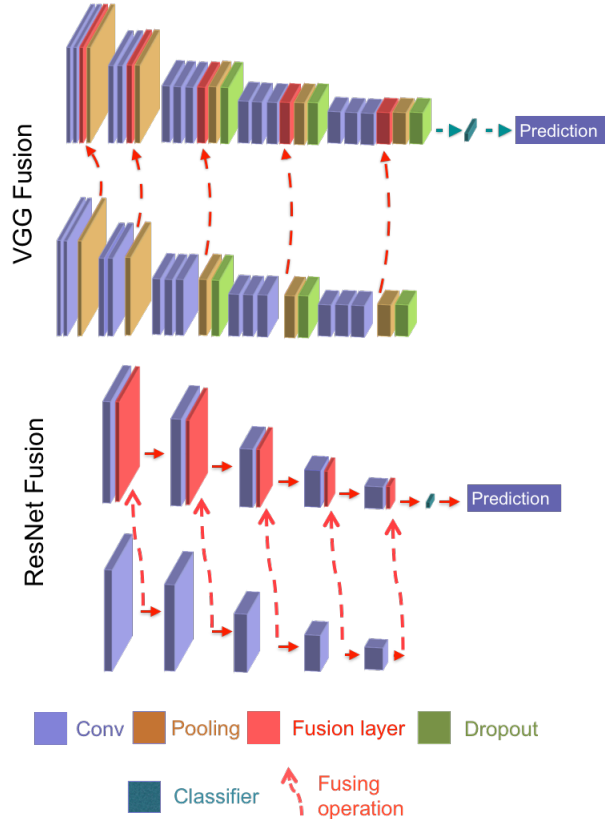


Figure 2. Architectures representing fusion in VGG and ResNet, two branches of each network are used to extract features and those features are fused in a hierarchy as the network goes deeper. Fusion in feature space activates relevant neurons in both branches of the network. These two architectures act as our baseline and are modified from FuseNet [9] and RedNet [13].

A common way to process temporally structured data is through the use of recurrent neural networks (RNNs) such as the long short term memory (LSTM) model [10]. For multimodal machine learning, Donahue *et.al.* combined CNNs with LSTMs to caption videos [5]. A more recent trend in deep learning is using attention based models where the model can dynamically weigh different portions of a sequence of data [1]. Attention based models have been used in multimodal applications as well [41].

Multimodal machine learning is also used for cross-modal data synthesis. These techniques are particularly prevalent in the medical field, as there are significant cost and privacy barriers in collecting medical data. For example, Huang *et. al.* and Vemulapalli *et. al.* were able to produce synthetic T2 weighted MRI images of the brain from T1 weighted MRI images and vice versa [12].

The advent of Generative Adversarial Networks (GANs) [8] has expanded interest in synthetic data generation and domain adaptation [18, 20] between modalities. Nie *et. al.* use conditional GANs (cGANs) to produce synthetic

CT images from MRI images [27]. Zhang *et. al.* synthesize data in a similar task using both the real and synthetic data to improve heart segmentation [42]. Shrivastava *et. al.* [36] use cGANs to make simulated images of the eye to appear more realistic, then use the realistic images to train a model to estimate eye gaze. Mahmood *et. al.* reverse this method by using GANs to convert real medical images to simulation-like images in order to train a network to estimate depth in endoscopy [18].

Data Fusion.

The use of multimodal data that is most relevant to our work is data fusion, in particular, fusing RGB and depth data for computer vision. One of the ways to classify data fusion methods is by early fusion, intermediate fusion, and late fusion. Generally, data is fused earlier when the modalities are correlated, and later when the modalities are less correlated [26]. Early, intermediate, and late fusion has all been used in various RGB-D applications. Eigen *et. al.* used early fusion by concatenating RGB and depth features after a single layer in a network that performed semantic segmentation [6]. Long *et. al.* used late fusion to perform RGB-D semantic segmentation [17] and Eitel *et. al.* used late fusion for RGBD object recognition [7]. Roy *et. al.* and Hazirbas *et. al.* fuse RGBD data at multiple stages which could theoretically accommodate both low and high-level correlations between RGB and depth data [32, 9]. Shahroudy *et. al.* explicitly extract both correlated and uncorrelated features for action recognition in RGB-D video [35]. Use of depth information has not been limited to fusing data in a neural network. Qi *et. al.* used depth data to construct a 3D graph that propagated non-local information and achieved state-of-the-art performance in semantic segmentation [30]. Wang *et. al.* modified the standard operations of convolution and pooling by weighing the contributions of neighboring pixels by their depth similarity [40]. This method also achieved competitive semantic segmentation results.

Vanishing Gradients in Multimodal Networks.

The best performing CNNs for visual object recognition tasks contain many convolutional layers. One issue with deep models is the vanishing gradient problem, where the back-propagation update dwindles by the time it reaches the early layers. Song *et. al.* demonstrated this problem in the context multimodal fusion and improved scene recognition by emphasizing the training of the bottom layers of a CNN [38]. Another way to combat the vanishing gradient problem is by directly connecting lower layers with higher ones. Mao *et. al.* implemented this idea by creating skip connections from the encoder to the decoder in their image restoration network [22]. Similarly, densenet was designed to send the output of a layer directly to every layer after it [11]. This allows backpropagation to reach the bottom layers much earlier than in models without skip connections.

3. Proposed Method: Multimodal Densenet

3.1. Theoretical Motivation

Multi-layer fusion network such as [9] are motivated by the fact that dual branch encoders with sequential feature fusion can pass a stronger signal which is representative of multiple modalities as compared to concatenation which may lose information about a specific modality. In order to maintain a strong signal from one layer to another representing pertinent information from multiple sources, adding activations at corresponding layers instead of concatenation can be more fruitful.

Heuristically, suppose the k^{th} feature map in the l^{th} layer is denoted by $\mathbf{h}_k^{(l)}$. Let the weights and biases for this feature and layer be denoted $W_K^{(l)} = [U_k^{(l)} \ V_K^{(l)}]^T$ and $b_k^{(l)} = [c_k^{(l)} \ d_k^{(l)}]^T$ respectively. Also, let $\mathbf{h} = [\mathbf{x}^T \ \mathbf{y}^T]^T$, where \mathbf{x} and \mathbf{y} are the learned features from the two modalities being fused. Assuming ReLU as the activation function,

$$\begin{aligned} \mathbf{h}_k^{(l+1)} &= \max(\mathbf{0}, W_k^{(l)} \mathbf{h} + y_k^{(l)}) & (1) \\ &= \max(\mathbf{0}, (U_k^{(l)} \mathbf{x}^{(l)} + V_k^{(l)} \mathbf{y}^{(l)} + (c_k^{(l)} + d_k^{(l)}))) & (2) \\ &\leq \max(\mathbf{0}, (U_k^{(l)} \mathbf{x}^{(l)} + c_k^{(l)})) + \max(\mathbf{0}, (V_k^{(l)} \mathbf{y}^{(l)} + d_k^{(l)})). & (3) \end{aligned}$$

Based on the inequality shown in Eq. 3 we can see that the fusion of the activations in $\psi(x)$ and $\phi(y)$ produces a stronger signal than the activation on concatenated inputs. In the context of scene classification tasks the fusing operation results in the strongest signals being passed through the final layer specifically at those places where the model finds useful information simultaneously in both modalities. In addition, the model preserves a signal, even though it may be a weaker one, when either modality contains useful information both for the learning of higher-level features and for the eventual classification of the image.

3.2. Network Architecture

The network architecture was conceived to utilize the strength of Densenet [11] for multimodal problems. The network is organized as a series of blocks, each composed of a series of 16 dense layers. Each dense layer is composed of the sequence of batch normalization, ReLU, bottleneck convolution, batch normalization, ReLU, and convolution. Height and width is preserved through a dense layer and the number of channels produced by the final convolution is known as the growth rate. Within the dense layer, the output from the bottleneck convolution is a fraction of the growth rate. The input to a dense layer is the concatenation of the outputs of all layers before it, within its block. This connection architecture combats the problem of vanishing

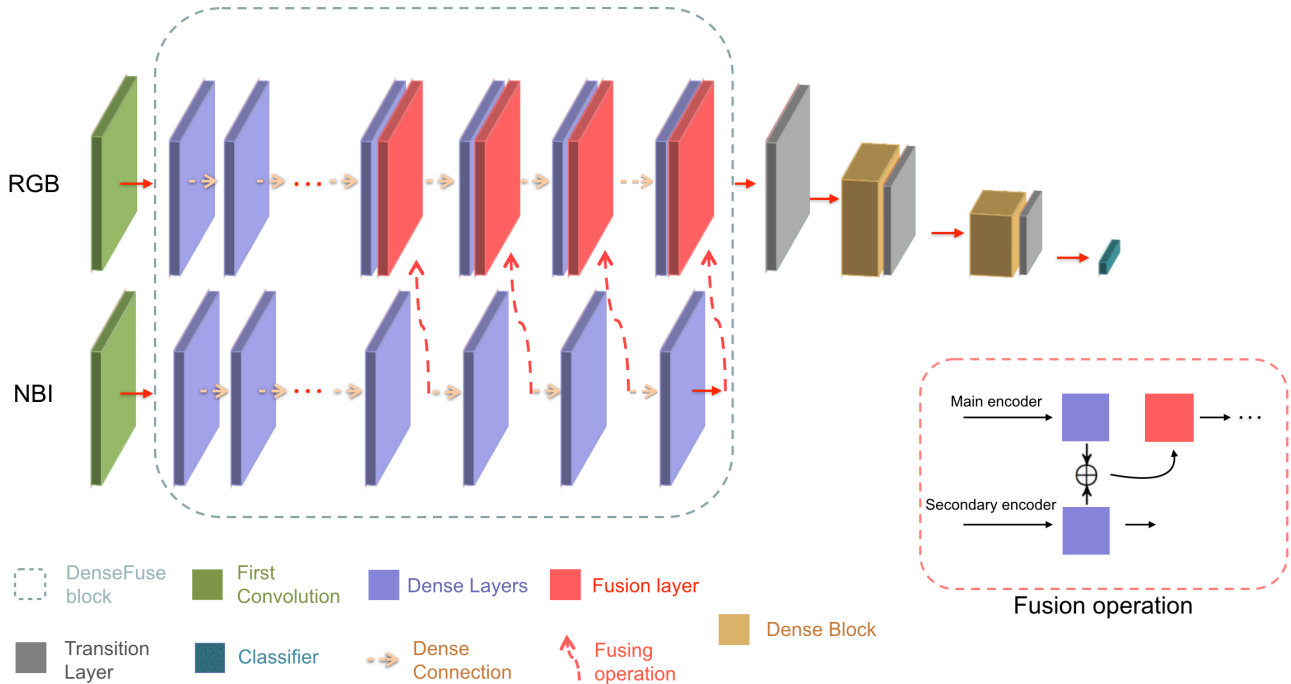


Figure 3. The network is composed of three densely connected blocks of 16 dense layers each. The first block has a channel for each modality, and constantly fuses information from the bottom channel into the top through element-wise addition. Within the dense blocks, each dense layer is composed of two consecutive sets of Batch Normalization, ReLU, and convolutional layers. Between dense blocks, transition layers include average pooling to increase the receptive field of subsequent layers.

gradients. Recent literature [38] has emphasized the importance of training low layers in multimodal deep learning and dense connectivity should theoretically address this need.

The first block of dense layers fuses the two sources of data similar to [9]. In this fuse block, there are two channels of dense layers, each processing an individual modality of data. During the first 8 dense layers, the RGB and depth channels proceed in parallel. Then, at each of the following 8 dense layers, the output from one secondary data channel is summed with the output of the primary data channel and is then used as input to the next layer in the primary channel. This is the key ingredient of the proposed multimodal architecture, such fusion combines the feature maps of the primary branch and the secondary branch. The rule of thumb of when to fuse multimodal data is to fuse early for highly correlated data and fuse late for uncorrelated data [31]. For example, when fusing RGB and depth data they can be sometimes correlated, perhaps at an objects edge, but sometimes uncorrelated, perhaps in the middle of a textured object, so its fusion should be an intermediate solution. Fusing two modalities over the course of several layers gives the model flexibility in how it combines information from multiple sources. The two blocks that come after the fuseblock consist of a single channel of 16 dense layers. Just between each block, there are transition layers

that consist of batch normalization, ReLU, convolution, and average pooling which downsamples the data to half its size in both height and width. Finally, the data passes through a ReLU, average pooling, fully connected, and softmax layer to make a classification determination. Although, the architecture presented here is only for scene classification, it may be extended for other tasks such as semantic segmentation.

3.3. Unpaired Multimodal Data

Often the two modalities being used can be unpaired, even though they may have information from the same scene or organ they may not be registered. Since using supervised and mathematical registration techniques can be tedious we propose using generative adversarial networks for finding a mapping between the two modalities. We used cycle consistency loss [43] with a conditional GAN to learn an unpaired mapping from white light to NBI images. Because of the consistency loss we also learn a reverse mapping from NBI images to white light images. Thus the reverse mapping is only used to train the forward mapping more effectively. Such an arrangement consists of four networks: G (White light to NBI), S (NBI to White light), D_N (discriminator for G), and D_W (discriminator for S). To train this framework for modality transfer with unpaired data, the overall objective consists of an adversarial loss

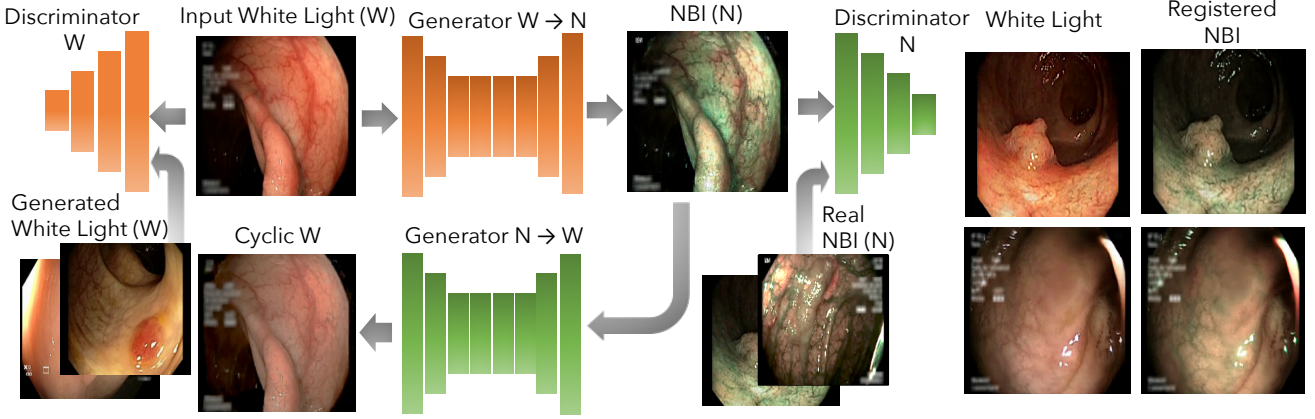


Figure 4. Unpaired mapping between white light and NBI images trained on unpaired data from the same scene. The architecture involves a dual-GAN setup with cycle consistency loss [43], two generators learn a mapping $G : W \rightarrow N$ and $S : N \rightarrow W$ and two discriminators classify the data as real/fake pairs.

term \mathcal{L}_{GAN} and a cycle consistency loss term \mathcal{L}_{cyc} to penalize unrealistic pairings between images. The adversarial loss is used to match the distribution of translated samples to that of the target distribution and can be expressed for both mapping functions. For the mapping $G : W \rightarrow N$ with discriminator D_N , we can express the objective as the binary cross entropy (BCE) loss of D_N in classifying real or fake, in which D_N and G play a *min-max* game to maximize and minimize this loss term respectively, the objective can be expressed as,

$$G^* \mathcal{L}_{GAN}(G, D_N) = \mathbb{E}_{n \sim p_{data}(n)} [\log D_N(n)] + \mathbb{E}_{w \sim p_{data}(w)} [\log(1 - D_N(G(w)))] \quad (4)$$

in which the generator G aims to find a mapping between white light and NBI images, *i.e.*, $G(m) \approx n$, while the discriminator D_N aims to distinguish generated *vs.* real NBI images. A similar objective can be expressed for $S : N \rightarrow M$,

$$S^* \mathcal{L}_{GAN}(S, D_W) = \mathbb{E}_{w \sim p_{data}(w)} [\log D_W(w)] + \mathbb{E}_{n \sim p_{data}(n)} [\log(1 - D_W(S(n)))] \quad (5)$$

The cycle consistency loss is used to incentivize a one-to-one mapping between samples in W and N , and that G and S act as inverse functions to each other. Specifically, the term ensures that the forward and back translations between the white light and NBI are lossless and cycle consistent, *i.e.*, $S(G(w)) \approx w$ (forward cycle consistency) and $G(S(N)) \approx N$ (backwards cycle consistency). The forward cycle loss term helps with refining NBI to be more realistic and avoid occlusions.

$$\mathcal{L}_{cyc}(G, S) = \lambda_n \mathbb{E}_{n \sim p_{data}(n)} [\|G(S(n)) - n\|_1] + \lambda_m \mathbb{E}_{m \sim p_{data}(m)} [\|S(G(m)) - m\|_1] \quad (6)$$

where λ controls the importance of the forward and backward cycle constraints. For domain transfer between white light and NBI images, we relaxed the λ_w term. The full objective for synthetic data generation can thus be written as,

$$G^*, S^* = \arg \min_{G, S} \arg \max_{D_N, D_W} \mathcal{L}_{GAN}(G, D_N) + \mathcal{L}_{GAN}(S, D_W) + \mathcal{L}_{cyc}(G, S) \quad (7)$$

4. Experiments

In this section, we evaluate the proposed multimodal network through extensive quantitative experimentation for three different multimodal classification tasks:

- Using white light RGB and corresponding depth for polyp classification in endoscopy data.
- Using white light and narrow band imaging (NBI) images for polyp classification in endoscopy data.
- Using white light RGB and corresponding depth images for anatomical landmark and pathology classification.

4.1. Datasets

We use two publicly available endoscopy datasets with ground truth labels:

ISIT-UMR Multimodal Polyp Classification Dataset.

We use the ISIT-UMR Multimodal classification dataset¹ that has been previously used for polyp classification tasks with classical machine learning methods [24]. The dataset consists of 76 polyps with both white light and NBI videos

¹http://www.depeca.uah.es/colonoscopy_dataset/

Method	Test Error ↓	Accuracy ↑	Recall ↑	Precision ↑	Specificity ↑	MCC ↑	F1 Score ↑
VGG16	0.265	0.825	0.705	0.791	0.855	0.614	0.720
VGG16-Fuse	0.160	0.893	0.789	0.714	0.937	0.660	0.732
ResNet50	0.157	0.895	0.802	0.831	0.903	0.720	0.809
ResNet50-Fuse	0.117	0.922	0.873	0.874	0.944	0.818	0.874
DenseNet	0.241	0.840	0.728	0.849	0.865	0.664	0.740
Multimodal Densenet	0.069	0.954	0.922	0.933	0.965	0.894	0.923

Table 1. Comparative analysis of different RGB and Depth Fusion Methods for Polyp Classification Data (3 Class Scene Classification Problem). VGG16, ResNet-50 and DenseNet are monomodal RGB networks while VGG16-Fuse, ResNet50-Fuse and Multimodal densenet are multimodal RGB-D networks.

Method	Test Error ↓	Accuracy ↑	Recall ↑	Precision ↑	Specificity ↑	MCC ↑	F1 Score ↑
VGG16	0.265	0.825	0.705	0.791	0.855	0.614	0.720
VGG16-Fuse	0.171	0.834	0.774	0.823	0.920	0.658	0.722
ResNet50	0.157	0.895	0.802	0.831	0.903	0.720	0.809
ResNet50-Fuse	0.128	0.903	0.852	0.844	0.918	0.806	0.836
DenseNet	0.241	0.840	0.728	0.849	0.865	0.664	0.740
Multimodal Densenet	0.084	0.926	0.916	0.927	0.944	0.877	0.908

Table 2. Comparative analysis of different Fusion Methods for fusing white light and narrow band imaging data for Polyp Classification (3 Class Scene Classification Problem). VGG16, ResNet-50 and DenseNet are monomodal RGB white light networks while VGG16-Fuse, ResNet50-Fuse and Multimodal densenet are multimodal white light + narrow band imaging networks.

from the same polyp. Each video orbits around a polyp capturing the texture and color information from different angles in both modalities. Each video has ground truth labels from histopathology and also has ground truth from multiple gastroenterologists. The dataset includes 3 classes of polyps: 15 serrated adenomas, 21 hyperplastic lesions and 40 adenoma. The length of each video is approximately 30 seconds and all videos are recorded at 26 frames/second. The white light and NBI videos were unregistered and were registered using the cycle-consistency adversarial paradigm described in the previous section. The depth for each frame was predicted using deep learning-based endoscopy depth estimation methods [19, 21]. 53 videos were used for training and 23 videos were used for test. The entire dataset was downsampled to 256×256 images for efficient processing.

Kvasir Landmark and Pathological Classification Dataset.

The Kvasir² dataset consists of several anatomical landmarks and pathological findings, we use seven classes, three for landmark detection (Z-line, Pylorus, Cecum) and three for pathological findings (Esophagitis, Polyps and Ulcerative Colitis) and a class for Normal colon mucosa. The dataset contains 1,000 unique images for each class, 7000 images were used in total. 70% of the data was used for training 10% for validation and 20% for testing. Depths were estimated for each frame using deep learning-based methods [19, 21].

²<http://datasets.simula.no/kvasir/>

4.2. Implementation Details

General Implementation Details. All networks were implemented using PyTorch 0.4 with Cuda 9.0. Google cloud with multiple Nvidia P100 GPUs was used to train all networks. All classification networks were trained using stochastic gradient decent (SGD) and images were down sampled 256×256 for efficient processing and to the batch size was constant at 16 for 200 epochs.

DenseNet. The network was trained for 200 epochs with an initial learning rate of 0.001 for the first 50 epochs and 0.0005 for another 50 epochs followed by 0.0002 for 80 epochs and eventually linearly decreased to zero over the remaining 20 epochs. The batch size was 16 and the weight decay parameter was set to 0.0001 and Nesterov momentum was 0.9. The dropout rate was set to 0.2.

Multimodal DenseNet. The network was trained for 200 epochs with an initial learning rate of 0.0002 for the first 40 epochs and 0.00005 for another 40 epochs followed by 0.00001 for 90 epochs and eventually linearly decreased to zero over the remaining 30 epochs. The batch size was 16 and the weight decay parameter was set to 0.0001 and Nesterov momentum was 0.9. The dropout rate was set to 0.2. Given this model is memory critical naive implementations may result in memory inefficiencies and memory-efficient DeneNets [28] may be used for to reduce such a possibility.

ResNet50 and ResNet50-Fuse. The standard ResNet architecture was used and the architecture presented in Fig. 2 was used to train ResNet-50 fuse for all three scene classification tasks. Both networks ran for 200 epochs at an

Method	Test Error ↓	Accuracy ↑	Recall ↑	Precision ↑	Specificity ↑	MCC ↑	F1 Score ↑
VGG16	0.375	0.701	0.681	0.683	0.764	0.608	0.648
VGG16-Fuse	0.306	0.748	0.718	0.728	0.799	0.621	0.716
ResNet50	0.282	0.781	0.762	0.760	0.773	0.653	0.697
ResNet50-Fuse	0.224	0.811	0.825	0.814	0.814	0.668	0.782
DenseNet	0.211	0.796	0.772	0.821	0.728	0.733	0.785
Multimodal Densenet	0.158	0.898	0.839	0.895	0.913	0.837	0.891

Table 3. Comparative analysis of different Fusion Methods for fusing RGB and depth data for Anatomical Landmark and Pathological Classification (6 Class Scene Classification Problem). VGG16, ResNet-50 and DenseNet are monomodal RGB networks while VGG16-Fuse, ResNet50-Fuse and Multimodal densenet are multimodal RGB-D networks.

initial learning rate of 0.001 which was decreased to 0.0005 after 50 epochs and was further linearly decreased for the remaining epochs. Weight decay was set to 0.0001 and the Nesterov momentum was 0.9 for both networks.

VGG16 and VGG16-Fuse. The standard VGG16 architecture and the architecture presented in Fig. 2 was used to train VGG16 fuse for all three scene classification tasks. Both networks ran for 200 epochs at an initial learning rate of 0.002 which was decreased to 0.0005 after 60 epochs and was further linearly decreased for the remaining epochs. Weight decay was set to 0.0001 and the Nesterov momentum was 0.9 for both networks.

Unpaired Multimodal Data Mapping Implementation.

The generator architectures contain two stride-2 convolutions, nine residual blocks and two functionally constrained convolutions with stride $\frac{1}{2}$. Reflection padding was used to minimize artifacts. The discriminator architecture was a simple classifier with three layers and the output was 70×70 with the aim to classify whether these overlapping patches were real or fake. As suggested in [43] a patch level discriminator has fewer parameters and is more easily applicable to various image sizes. We observed that larger size images needed more residual blocks for efficient convergence. The GAN training was stabilized to prevent mode collapse by using spectral normalization [25]. For all experiments $\lambda_n = 70$ and $\lambda_w = 10$. Adam solver [14] was used to solve the optimization problem with a batch size of 1 which was experimentally determined. A total of 300 epochs were used. The learning rate was set to 0.0002 for the first 150 epochs and linearly decayed to zero for the remaining 150 epochs. In practice the objective function is divided by two when optimizing the discriminator *i.e.*, the discriminator learns at a lower rate as compared to the generator. All networks were trained from scratch with no prior knowledge and weights were initialized from a Gaussian distribution with a mean and standard deviation of 0 and 0.02 respectively.

5. Results

5.1. Evaluation Metrics

We used seven different evaluation metrics to evaluate the three different classification problems. These include

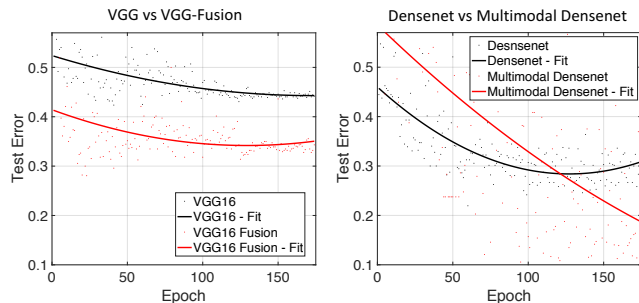


Figure 5. A comparative analysis of VGG16 and VGG16 fusion (Fig. 2) vs DenseNet and Multimodal Densenet. It can be seen that RGB-D classification works better than RGB classification in both networks. Although multimodal densenet needs more epochs to realize its full potential it outperforms VGG16 fusion.

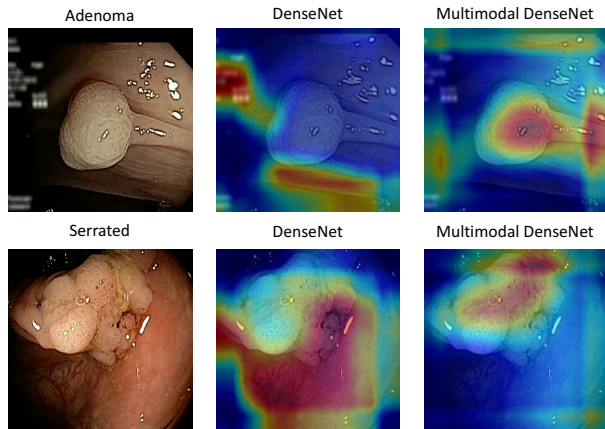


Figure 6. Gradient Class Activation Maps (Grad-CAM) for DenseNet (RGB) and Multimodal DenseNet (RGB-D) showing regions used for classification when trained with the same amount of data. It can clearly be seen that Multimodal Densenet focuses on the polyps.

overall test error, accuracy, precision (ratio of samples that are correctly identified as positive), recall or sensitivity (ratio of samples that are correctly identified as positive among all existing positive samples), specificity (ratio of negatives that are correctly identified), Matthews correlation coefficient (MCC) [23], and the F1 score (harmonic mean of the precision and recall). MCC was first proposed for binary

problems but has since been extended for multi-class problems and is often referred to as the single most informative metric for classification problems [3].

5.2. 3-Class Polyp Characterization using RGB White Light images and Depth

During gastrointestinal screening physicians predict the depth of a polyp and subjectively assess the need for biopsy. Here we fuse information from predicted and white light RGB images and demonstrate that fusion depth can improve objective polyp classification. Table 1 shows the results for the three class classification problem with and without depth fusion using three different fusion networks. This comparative analysis is designed to compare standard multi-layer fusion networks. We do not compare by simply concatenating depth and RGB information because it has previously been shown that multi-layer fusion always outperforms concatenation [9, 13].

The F_1 score for RGB-D Multimodal Densenet is by 24.72% greater than that for DenseNet. The percentage change for VGG16-Fuse as compare to VGG16 is 4.28% and that for ResNet-50-Fuse as compared to ResNet-50 is 8.03%. This clearly indicates that our proposed Multimodal Densenet is capable to extracting information from both RGB information and depth simultaneously as compared to other networks.

A comparative analysis of the test error with respect to epochs has been shown in Fig. 5. The comparison is between VGG16 fusion and multimodal densenet. As demonstrated our proposed multimodal densenet outperforms VGG16, VGG16-Fusion and Densenets. Although, it should be noted that multimodal densenets do require more training as compared to monomodal and other relatively shallow multi-layer fusion counterparts.

Gradient Class Activation Maps (Grad-CAM): In order to further demonstrate the superiority of multimodal densenet over its monomodal counterpart and to determine the accuracy of our training we visualized the features being used to make classification determinations by our networks. This was done by visualizing gradient class activation maps for each class [34]. It can be seen that given the small amount of data we used densenet often makes determinations based on regions around the polyp rather than directly on the surface of the polyp. However, when depth was fused using and the proposed multimodal architecture was used the classification label was determined from the surface of the polyp possibly using color and texture of the lumen. Indeed, in most cases densenet is capable of making the right determinations, this analysis only shows cases where RGB densenets fail and RGB-D multimodal densenet is capable of classifying the polyp accurately.

5.3. 3-Class Polyp Characterization using White Light and NBI

We further extend our quantitative analysis by exploring the fusion of narrow band imaging with white light endoscopy images. During gastrointestinal screening gastroenterologists often switch between white light and narrow band endoscopy to characterize a polyp and determine the need for a biopsy. Using the dataset described earlier we had videos from both modalities which were unpaired and unregistered. We registered them using the adversarial setup with cycle consistency loss described in section 3.3 (Fig. 4). For comparative analysis registered images from white light and narrow band imaging were fused using multimodal densenet, VGG16-Fuse and ResNet-50-Fuse baselines (Fig. 2). The results are shown in Table 2. The F_1 score for white light + NBI multimodal Densenet is by 8.03% greater than that for DenseNet. The percentage change for VGG16-Fuse as compare to VGG16 is 3.33% and that for ResNet-50-Fuse as compared to ResNet-50 is 1.66%. This clearly indicates that our proposed multimodal densenet architecture is capable to extracting information from both white light and NBI simultaneously as compared to other fusion networks.

5.4. 7-Class Anatomical Landmarks and Pathological Classification

Capsule endoscopy is an efficient method for upper gastrointestinal screening. However, the images acquired from this method are screened after the procedure is complete and the physician often spends several minutes watching a video in high speed, during this process it is possible to miss polyps and anatomical landmarks. Here, we should that it is possible to objectively classify anatomical landmarks and pathological findings using a 7-class classification problem. We further show that it is possible to fuse depth with RGB images to get improved results using the proposed multimodal densenet architecture (Table 3).

6. Conclusions

In this paper, we present a new architecture to fuse information from multiple medical imaging modalities. We propose using a densenet style architecture and fusing the multimodal information in the last eight layers of the first dense block, hence harnessing the benefits of both multi-layer fusion and densely connected networks. We further demonstrate that unpaired information from the same scene or organ can be used for such fusion if the domains are aligned using adversarial training and cycle consistency loss. We demonstrate that our proposed architecture outperforms existing fusion strategies and architectures for three multimodal scene classification tasks: (1) RGB-D polyp classification in endoscopy (2) White light-NBI polyp classification in endoscopy (3) RGB-D anatomical landmark and

pathological classification in endoscopy.

References

- [1] J. Ba, V. Mnih, and K. Kavukcuoglu. Multiple object recognition with visual attention. *arXiv preprint arXiv:1412.7755*, 2014. 2
- [2] T. Baltrušaitis, C. Ahuja, and L.-P. Morency. Multimodal machine learning: A survey and taxonomy. *IEEE Transactions on Pattern Analysis and Machine Intelligence*, 2018. 2
- [3] D. Chicco. Ten quick tips for machine learning in computational biology. *BioData mining*, 10(1):35, 2017. 8
- [4] W. L. Curvers, R. Singh, L. W.-K. Song, H. C. Wolfson, K. Ragnath, K. Wang, M. B. Wallace, P. Fockens, and J. Bergman. Endoscopic tri-modal imaging for detection of early neoplasia in barretts oesophagus: a multi-centre feasibility study using high-resolution endoscopy, autofluorescence imaging and narrow band imaging incorporated in one endoscopy system. *Gut*, 57(2):167–172, 2008. 2
- [5] J. Donahue, L. Anne Hendricks, S. Guadarrama, M. Rohrbach, S. Venugopalan, K. Saenko, and T. Darrell. Long-term recurrent convolutional networks for visual recognition and description. In *Proceedings of the IEEE conference on computer vision and pattern recognition*, pages 2625–2634, 2015. 2
- [6] D. Eigen and R. Fergus. Predicting depth, surface normals and semantic labels with a common multi-scale convolutional architecture. In *Proceedings of the IEEE International Conference on Computer Vision*, pages 2650–2658, 2015. 3
- [7] A. Eitel, J. T. Springenberg, L. Spinello, M. Riedmiller, and W. Burgard. Multimodal deep learning for robust rgb-d object recognition. In *Intelligent Robots and Systems (IROS), 2015 IEEE/RSJ International Conference on*, pages 681–687. IEEE, 2015. 3
- [8] I. Goodfellow, J. Pouget-Abadie, M. Mirza, B. Xu, D. Warde-Farley, S. Ozair, A. Courville, and Y. Bengio. Generative adversarial nets. In *Advances in neural information processing systems*, pages 2672–2680, 2014. 2
- [9] C. Hazirbas, L. Ma, C. Domokos, and D. Cremers. Fusetnet: Incorporating depth into semantic segmentation via fusion-based cnn architecture. In *Asian Conference on Computer Vision*, pages 213–228. Springer, 2016. 1, 2, 3, 4, 8
- [10] S. Hochreiter and J. Schmidhuber. Long short-term memory. *Neural computation*, 9(8):1735–1780, 1997. 2
- [11] G. Huang, Z. Liu, L. Van Der Maaten, and K. Q. Weinberger. Densely connected convolutional networks. In *CVPR*, volume 1, page 3, 2017. 3
- [12] X. Huang, M.-Y. Liu, S. Belongie, and J. Kautz. Multimodal unsupervised image-to-image translation. *arXiv preprint arXiv:1804.04732*, 2018. 2
- [13] J. Jiang, L. Zheng, F. Luo, and Z. Zhang. Rednet: Residual encoder-decoder network for indoor rgb-d semantic segmentation. *arXiv preprint arXiv:1806.01054*, 2018. 1, 2, 8
- [14] D. P. Kingma and J. Ba. Adam: A method for stochastic optimization. *arXiv preprint arXiv:1412.6980*, 2014. 7
- [15] R. Kiros, R. Salakhutdinov, and R. Zemel. Multimodal neural language models. In *International Conference on Machine Learning*, pages 595–603, 2014. 2
- [16] A. Krizhevsky, I. Sutskever, and G. E. Hinton. Imagenet classification with deep convolutional neural networks. In *Advances in neural information processing systems*, pages 1097–1105, 2012. 2
- [17] J. Long, E. Shelhamer, and T. Darrell. Fully convolutional networks for semantic segmentation. In *Proceedings of the IEEE conference on computer vision and pattern recognition*, pages 3431–3440, 2015. 3
- [18] F. Mahmood, R. Chen, and N. J. Durr. Unsupervised reverse domain adaptation for synthetic medical images via adversarial training. *IEEE Transactions on Medical Imaging*, 2018. 2, 3
- [19] F. Mahmood, R. Chen, S. Sudarsky, D. Yu, and N. J. Durr. Deep learning with cinematic rendering-fine-tuning deep neural networks using photorealistic medical images. *Physics in Medicine and Biology*, 2018. 6
- [20] F. Mahmood and N. J. Durr. Deep learning and conditional random fields-based depth estimation and topographical reconstruction from conventional endoscopy. *Medical Image Analysis*, 2018. 2
- [21] F. Mahmood and N. J. Durr. Topographical reconstructions from monocular optical colonoscopy images via deep learning. In *Biomedical Imaging (ISBI 2018), 2018 IEEE 15th International Symposium on*, pages 216–219. IEEE, 2018. 6
- [22] X.-J. Mao, C. Shen, and Y.-B. Yang. Image restoration using convolutional auto-encoders with symmetric skip connections. *arXiv preprint arXiv:1606.08921*, 2016. 3
- [23] D. Matthews, J. Hosker, A. Rudenski, B. Naylor, D. Treacher, and R. Turner. Homeostasis model assessment: insulin resistance and β -cell function from fasting plasma glucose and insulin concentrations in man. *Diabetologia*, 28(7):412–419, 1985. 7
- [24] P. Mesejo, D. Pizarro, A. Abergel, O. Rouquette, S. Borchia, L. Poincloux, and A. Bartoli. Computer-aided classification of gastrointestinal lesions in regular colonoscopy. *IEEE transactions on medical imaging*, 35(9):2051–2063, 2016. 5
- [25] T. Miyato, T. Kataoka, M. Koyama, and Y. Yoshida. Spectral normalization for generative adversarial networks. *arXiv preprint arXiv:1802.05957*, 2018. 7
- [26] J. Ngiam, A. Khosla, M. Kim, J. Nam, H. Lee, and A. Y. Ng. Multimodal deep learning. In *Proceedings of the 28th international conference on machine learning (ICML-11)*, pages 689–696, 2011. 2, 3
- [27] D. Nie, R. Trullo, J. Lian, C. Petitjean, S. Ruan, Q. Wang, and D. Shen. Medical image synthesis with context-aware generative adversarial networks. In *International Conference on Medical Image Computing and Computer-Assisted Intervention*, pages 417–425. Springer, 2017. 3
- [28] G. Pleiss, D. Chen, G. Huang, T. Li, L. van der Maaten, and K. Q. Weinberger. Memory-efficient implementation of densenets. *arXiv preprint arXiv:1707.06990*, 2017. 6
- [29] S. Poria, E. Cambria, and A. Gelbukh. Deep convolutional neural network textual features and multiple kernel learning for utterance-level multimodal sentiment analysis. In *Proceedings of the 2015 conference on empirical methods in natural language processing*, pages 2539–2544, 2015. 1

- [30] X. Qi, R. Liao, J. Jia, S. Fidler, and R. Urtasun. 3d graph neural networks for rgb-d semantic segmentation. In *Proceedings of the IEEE Conference on Computer Vision and Pattern Recognition*, pages 5199–5208, 2017. 3
- [31] D. Ramachandram and G. W. Taylor. Deep multimodal learning: A survey on recent advances and trends. *IEEE Signal Processing Magazine*, 34(6):96–108, 2017. 4
- [32] A. Roy and S. Todorovic. A multi-scale cnn for affordance segmentation in rgb images. In *European Conference on Computer Vision*, pages 186–201. Springer, 2016. 3
- [33] C. Sebastian, B. Boom, T. van Lankveld, E. Bondarev, and P. H. De With. Bootstrapped cnns for building segmentation on rgb-d aerial imagery. *arXiv preprint arXiv:1810.03570*, 2018. 1
- [34] R. R. Selvaraju, M. Cogswell, A. Das, R. Vedantam, D. Parikh, D. Batra, et al. Grad-cam: Visual explanations from deep networks via gradient-based localization. In *ICCV*, pages 618–626, 2017. 8
- [35] A. Shahroudy, T.-T. Ng, Y. Gong, and G. Wang. Deep multimodal feature analysis for action recognition in rgb+ d videos. *IEEE Transactions on Pattern Analysis and Machine Intelligence*, 40(5):1045–1058, 2018. 3
- [36] A. Shrivastava, T. Pfister, O. Tuzel, J. Susskind, W. Wang, and R. Webb. Learning from simulated and unsupervised images through adversarial training. In *CVPR*, volume 2, page 5, 2017. 3
- [37] R. Socher, M. Ganjoo, C. D. Manning, and A. Ng. Zero-shot learning through cross-modal transfer. In *Advances in neural information processing systems*, pages 935–943, 2013. 2
- [38] X. Song, L. Herranz, and S. Jiang. Depth cnns for rgb-d scene recognition: Learning from scratch better than transferring from rgb-cnns. In *AAAI*, pages 4271–4277, 2017. 3, 4
- [39] N. Srivastava and R. R. Salakhutdinov. Multimodal learning with deep boltzmann machines. In *Advances in neural information processing systems*, pages 2222–2230, 2012. 2
- [40] W. Wang and U. Neumann. Depth-aware cnn for rgb-d segmentation. *arXiv preprint arXiv:1803.06791*, 2018. 3
- [41] Z. Yang, X. He, J. Gao, L. Deng, and A. Smola. Stacked attention networks for image question answering. In *Proceedings of the IEEE Conference on Computer Vision and Pattern Recognition*, pages 21–29, 2016. 2
- [42] Z. Zhang, L. Yang, and Y. Zheng. Translating and segmenting multimodal medical volumes with cycle-and shapeconsistency generative adversarial network. In *Proceedings of the IEEE Conference on Computer Vision and Pattern Recognition*, pages 9242–9251, 2018. 3
- [43] J.-Y. Zhu, T. Park, P. Isola, and A. A. Efros. Unpaired image-to-image translation using cycle-consistent adversarial networks. *arXiv preprint*, 2017. 4, 5, 7